06

Detonation synthesis of metal nanoparticles and study of their morphology

© N.A. Khlebanovsky,[1,2] B.L. Moroz,[1] A.O. Kashkarov,[2] K.A. Ten,[2] Ya.L. Lukyanov,[2] E.Yu. Gerasimov,[3] M.R. Sharafutdinov[4]

[1] Novosibirsk State University,
630090 Novosibirsk, Russia
[2] Lavrentyev Institute of Hydrodynamics, Siberian Branch, Russian Academy of Sciences,
630090 Novosibirsk, Russia
[3] Boreskov Institute of Catalysis, Siberian Branch of RAS,
630090 Novosibirsk, Russia
[4] Institute of Solid State Chemistry and Mechanochemistry, Siberian Branch, Russian Academy of Sciences,
630128 Novosibirsk, Russia
e-mail: n.khlebanovskii@g.nsu.ru

Received November 6, 2024
Revised November 6, 2024
Accepted November 6, 2024.

The influence of the characteristics of explosive composites based on PETN and RDX containing Fe(II) oxalate and Cu(II) oxalate and acetate on the morphology of metal-containing nanoparticles formed as a result of detonation was studied using structural analysis methods. It was shown that the composition of the decomposition products of Fe(II) oxalate under explosion conditions is similar to the composition of the products of its thermal decomposition. In contrast, metallic copper and Cu(II) oxide, which are formed during their thermal decomposition, are absent among the decomposition products of Cu(II) oxalate and acetate. For charges containing an additive of Fe(II) oxalate, it was found that the charge density has a stronger effect on the average size of iron-containing nanoparticles and their size distribution than the mass fraction of the additive.

Keywords: detonation products, detonation synthesis, nanoparticle morphology, metal nanoparticles.

DOI: 10.61011/TP.2025.02.60840.367-24

Introduction

Detonation synthesis of metallic nanoparticles involves decomposition of substances containing metals using explosion energy. A qualitative model of this process was discussed in [1]. Behind the detonation front of explosive composite materials, thermal decomposition of metal-containing precursor molecules likely takes place and formation of metallic particles then occurs in the relief wave according to the diffusion mechanism. Compared with other metallic nanoparticle synthesis techniques such as laser evaporation followed by condensation [2], electroexplosive metal wire evaporation [3] or local electron irradiation of crystals [4], detonation synthesis is performed in substantially different conditions. Detonation front of explosive substances (ES) is characterized by pressures of several tens of GPa, temperature of several thousands of degrees, high density of detonation products and short synthesis time that is estimated as units of microseconds. Such extreme synthesis conditions are expected to be expressed through the morphology of produced nanoparticles.

It has been shown before that the sizes of produced nanoparticles are in a quite wide range, for example, silver nanoparticles with sizes from 3 nm to 20 nm were synthesized by means of detonation of a silver stearate and pentraerythritol tetranitrate (PETN) mixture in [5]. In [6], detonation of TATB and BTP mixtures with silver caprylate, tetraamminegold(III) nitrate, nickel(II) stearate or palladium(II) stearate in different proportions with ES produced silver nanoparticles with diameters from 2 nm to 60 nm, nickel nanoparticles with sizes from 3 nm to 5 nm, palladium nanoparticles with sizes from 1 nm to 3 nm and gold nanoparticles with sizes from 2 nm to 25 nm. In [7], detonation of PETN charge containing 15 wt.% of silver stearate was used to synthesize silver particles with sizes from 3 nm to 20 nm coated with a thin amorphous carbon layer. Similar results were also later obtained by other authors: in particular, detonation of the picric acid and ferrocene mixture was used to synthesize 5–20 nm Fe nanoparticles [8], and detonation of hydrogen, air and ferrocene mixtures containing different amounts of metalorganic precursor was used to produce Fe nanoparticles with mean diameters of 30–40 nm [9]. In [10], explosions of PETN and hexogen mixed with Fe(III) and Ni(II) nitrates produced ferronickel nanoparticles with diameters from 10 nm to 50 nm. Results of already performed studies suggest that the sizes of metallic nanoparticles synthesized in detonation conditions depend on the ES to be used, chemical nature of metal and ligands included in the metal-containing compound, precursor, explosive composite material manufacturing process and mass fraction of metal in the composite material.

In this study, detonation synthesis was performed using the following metal-containing precursors: Fe(II) $FeC_2O_4 \cdot 2H_2O$ oxalate, Cu(II) $CuC_2O_4 \cdot 0.5H_2O$ oxalate and Cu(II) $Cu(CH_3COO)_2 \cdot H_2O$ acetate. According to the literature data [11,12], Fe(II) and Cu(II) oxalates, when heated to 300−400°C, loose crystallization water and are decomposed to form the metal oxide:

$$MC_2O_4 \rightarrow MO + CO\uparrow + CO_2\uparrow, \text{ where } M = Fe(II), Cu(II).$$

In conditions of thermal decomposition of MC_2O_4, secondary reactions involving CO may take place such as MO reduction to metal

$$MO + CO \rightarrow M^\circ + CO_2,$$

and CO disproportionation (Boudouard reaction)

$$2CO \rightarrow C + CO_2.$$

Metallic iron nanoparticles are the Boudouard reaction catalysts, therefore nonstoichiometric iron carbides often occur among the thermolysis products of MC_2O_4. Moreover, FeO in the presence of oxygen can be oxidized to Fe_3O_4 and/or Fe_2O_3. Probability of secondary transformations of MO grows considerably as the temperature and pressure increase. Cu(II) acetate, when heated in oxygen-containing atmosphere, is decomposed to form CuO:

$$Cu(CH_3COO)_2 + 4O_2 \rightarrow CuO + 4CO_2\uparrow + 3H_2O,$$

Cu_2O and Cu° are also formed in an inert atmosphere or with small amount of oxygen [13,14].

PETN and hexogen were used as ES that give a small amount of condensed carbon during detonation. Consequently, solid detonation products contained only metallic and/or metal oxide particles and a small amount of condensed carbon that simplified the diffraction analysis of these products. For the purpose of experiments, the mass fraction of metal-containing precursor in an explosive composite material and charge density were varied. Thus, the influence of only these factors on nanoparticle sizes was studied with other factors being unchanged.

1. Fabrication of the explosive composite material and detonation synthesis

The explosive composite material was made using metal-containing precursors $FeC_2O_4 \cdot 2H_2O$ with granule sizes of 10−20 μm and $CuC_2O_4 \cdot 0.5H_2O$ with granule sizes of about 50−200 nm and an explosive substance - PETN. The MERLIN Compact VP scanning electron microscope was used to make and examine microphotographs of original Fe(II) and Cu(II) oxalate powders. Fe(II) oxalate granules are crystallized well enough, have pronounced facets and a near-cubic shape, and Cu(II) oxalate granules contain finer particles and have a ball-shaped shape. Unlike Fe(II) oxalate granules, Cu(II) oxalate granules are also more prone to agglomeration.

Table 1. Composition and density of FeC_2O_4/PETN charges

№ and type of charge	1 (pressed)	2 (pressed)	3 (loose)
Mass fraction FeC_2O_4, %	3	6	3
Density,g/cm^3	1.58	1.55	≈ 1.1

A salting out method was used for uniform introduction of Fe(II) and Cu(II) oxalate powders into the explosive substance. A Fe(II) or Cu(II) oxalate powder water suspension was prepared initially. Suspension uniformity was achieved by preliminary ultrasonic bath treatment followed by vigorous stirring using a magnetic stirrer. Then, a PETN acetone solution was poured into the continuously stirred suspension. As a result of sharp decrease in PETN solubility in water-diluted acetone, it precipitates to form granules with approximately the same size as that of the Fe(II) oxalate granules (from units to tens of microns). Irregularities in the form of oxalate granules are supposed to serve as centers of crystallization of PETN, and continuous vigorous stirring facilitates uniform mixing of PETN with the metal-containing compound. The precipitate after filtering and drying was used as an explosive composite material. PETN and Fe(II) or Cu(II) oxalate mixtures with various weight ratios were prepared by varying the oxalate content in the water suspension.

According to the scanning electron microscopy data, Fe(II) oxalate granules or small granule agglomerates are distributed quite uniformly in the explosive composite powder. Individual FeC_2O_4 granules are well distinguished against the needle-plate-shaped granules typical of the reprecipitated PETN. Pressed cylindrical charges 20 mm in diameter and a loose charge (composition and density of these charges are shown in Table 1) were made from the prepared explosive composites with different mass fraction of FeC_2O_4.

Cu(II) oxalate crystals that are finer than PETN granules are also quite uniformly distributed on their surface. Hexogen-based composite material with Cu(II) oxalate additive was prepared in the same way as the CuC_2O_4/PETN composite material by salting hexogen out of the acetone solution by water in the presence of CuC_2O_4 crystals. The PETN or hexogen and copper acetate mixtures were prepared by mechanical stirring of ES and $Cu(CH_3COO)_2$ powders because copper acetate, unlike copper oxalate, is very soluble in water. The PETN/hexogen and copper salt mixtures were used to make loose type charges with the density of ~ 1.1 g/cm^3 whose composition is shown in Table 2.

The scheme of detonation synthesis experiment is identical to that used in [15]. The experimental assembly was placed into a ≈ 1 m^3 stainless steel explosion chamber to

Table 2. List of loose charges made with a copper salt additive (3 wt.%)

Charge №	1	2	3	4
ES	PETN	hexogen	PETN	hexogen
Copper-containing component	CuC_2O_4	CuC_2O_4	$Cu(CH_3COO)_2$	$Cu(CH_3COO)_2$

reduce the amount of metallic impurities that may occur in the solid detonation product after the chamber wall fracture. The explosive composite material and initiator consisting of a detonator and primer (PETN without metal-containing additive) were placed into a distilled water ice shell. The ice shall is needed to decelerate the explosion products before their collision with the explosion chamber walls, avoid excessive heating and preserve the products in their initial form as much as possible [16]. With the general weight of each charge of about 15–20 g, the weight of the ice shell was about 1 kg. After the detonation, the explosion chamber was opened, condensed explosion products (in the form of water suspension) were collected, separated from water by vacuum filtering and dried in air with moderate heating.

2. Findings and discussion

2.1. Transmission electron microscopy of iron-containing explosion products

Condensed explosion product images made on the JEM 2010 transmission electron microscope with line resolution equal to 1.4 Åare shown in Figure 1.

Microphotographs of the preserved explosion products of all iron-containing charged (Figure 1) show contrast images of ball-shaped metallic or metal-oxide particles with sizes from 5 nm to 200 nm together with smeared images of detonation carbon globules that constitute a small part of all studied samples. According to visual estimate, the largest amount of detonation carbon is contained in a sample made from the loose charge.

It can be also seen from the high-magnification microphotographs of the preserved explosion products that the ball-shaped nanoparticles are darker in the center and brighter near the edge, and also have a crystal lattice on their surface. This may indicate that the particles have metallic and metal oxide nuclei and are coated with crystalline carbon, which corresponds to the nanoparticle formation mechanism described in [1].

The structural analysis using the small-angle X-ray scattering technique conducted as described in [17] has shown that explosion products of all samples consist primarily of large ball-shaped iron-containing particle with insignificant inclusion of finer carbon particle and globule agglomerates. This agrees well with the microscopy data and suggests that these patterns are typical of the total amount of explosion products. The small-angle X-ray scattering signal was

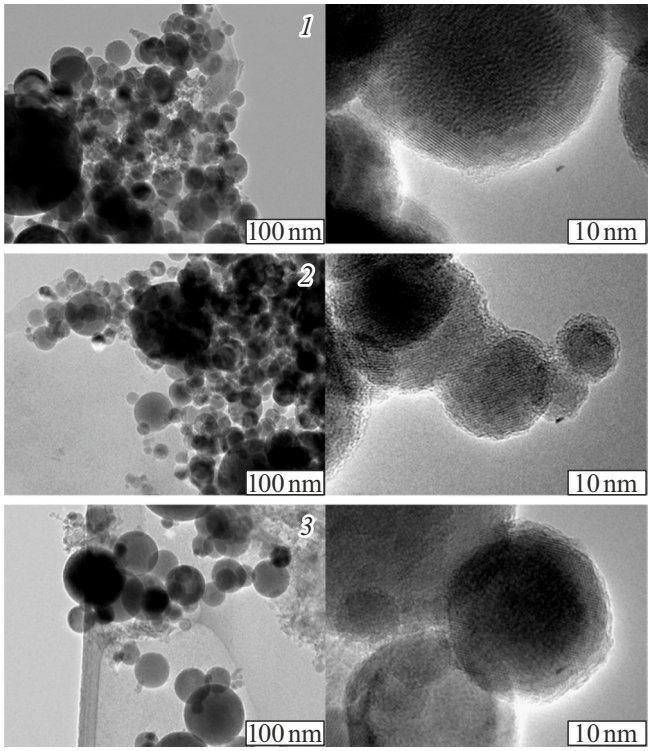

Figure 1. Microphotographs of products obtained from the explosion of: *1* — pressed 6% FeC_2O_4/PETN charge; *2* — pressed 3% FeC_2O_4/PETN charge; *3* — loose 3% FeC_2O_4/PETN charge.

recorded by the VEPP-3 acceleration system at the Institute of Nuclear Physics, Siberian Branch, Russian Academy of Sciences.

Images with large number 2 of metal-containing particles and particle size distribution that is more typical of each of the image series were chosen for the assay. Metal-containing particle dimensions were determined by measuring their image diameters. Figure 2 shows the particle size distribution histograms and approximation by lognormal distribution curves. Average diameters (d_l) of iron-containing particles in the studied samples calculated as follows: $d_l = \Sigma(d_i)/N$ (where d_i is the particle image diameter on the microphotograph, N is the total number of measured particles), and quantities that characterize the agreement between the experimental particle size distributions and the describing model (lognormal distribution) are shown in Table 3. Coefficients of determination R^2 of the approximation made for the detonation products of all FeC_2O_4/PETN charges are close to 1, however, the chi-square criterion for unpressed

Table 3. Calculated Chapman–Jouguet detonation variables for the FeC_2O_4/PETN charges with different densities, number-average diameters (d_l) of iron-containing particles

Charge composition	3 wt.% FeC_2O_4/PETN (pressed)	6 wt.% FeC_2O_4/PETN (pressed)	3 wt.% FeC_2O_4/PETN (loose)
ES density for calculation of the Chapman–Jouguet variables, g/cm^3	1.53	1.45	1.05
Chapman–Jouguet pressure, GPa	20.8	18.3	8.2
Chapman–Jouguet temperature, K	4281	4330	4407
Average diameters d_l, nm	31	33	37

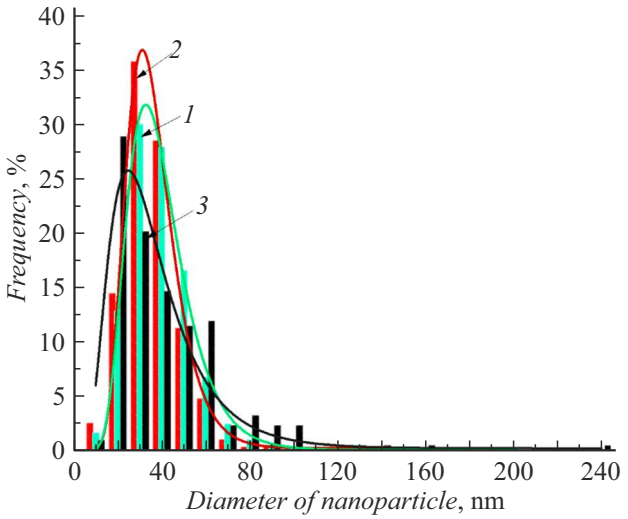

Figure 2. Size distributions of iron-containing particles in samples made by the detonation synthesis from the FeC_2O_4/PETN charges, and their approximating lognormal distribution curves: *1* — pressed 6% FeC_2O_4/PETN charge; *2* — pressed 3% FeC_2O_4/PETN charge; *3* — loose 3% FeC_2O_4/PETN charge.

charge detonation product differs from zero much larger than in other two cases. This indicates the feasibility of using the lognormal approximation of metal-containing particle size distribution in solid detonation products of pressed charges and shows that size distribution of these particles in a solid detonation product of unpressed charge has a somewhat different form. Nevertheless, Figure 2 in all cases uses the same type of approximation because this is convenient for comparison of the results. It can be seen that lognormal particle size distribution curve peaks in the detonation products of pressed charges with different content of FeC_2O_4 almost coincide with each other, while the peak of particle size distribution in the detonation product of loose density charge is lower and to the left of them. At the same time, this distribution has a long „tail“ extended towards larger diameters,therefore d_l in this case is higher than in two other cases ($d_l = 37$ nm compared with 31 nm and 33 nm).

Using the detonation wave calculator for calculation of equilibrium Chapman–Jouguet detonation parameters of energy-related materials [18], the Chapman–Jouguet pressure and temperature were calculated for the charges. For the purpose of calculation, the charge density was set equal to that of the studied samples less the contribution of the metal-containing precursor because it was supposed to be an inert additive that didn't affect the detonation process. Calculated detonation pressures and temperatures of the FeC_2O_4/PETN charges with different densities are also shown in Table 3.

It can be seen from the data in Table 3 that, as the charge density decreases, the detonation temperature increases not too much, and the pressure decreases significantly (by 2.2–2.5 times). Charges with different content of FeC_2O_4 (3% and 6%) having approximately the same density (1.58 g/cm3 and 1.55 g/cm^3, respectively) produced iron-containing nanoparticles with the same type of size distribution (Figure 2) and approximately the same mean size ($d_l = 31$ and 33 nm, Table 3), while the detonation of the unpressed 3% FeC_2O_4/PETN charge with a density of 1.1 g/cm^3 gave a product with a wider size distribution of iron-containing particles that included a considerable amount of large crystallites with a diameter of 80–100 nm and, consequently, with a large mean size of these particles ($d_l = 37$ nm). This data suggests that, for the adopted explosive composite fabrication process, mass content of FeC_2O_4 in the composite material has a low influence on the mean size of metal-containing nanoparticles produced during explosion and on the type of size distribution, but the density of original charge has a much higher influence. This in turn suggests that the Chapman–Jouguet pressure is the key variable that affects the dispersiveness of metal-containing particles synthesized in the detonation conditions and, as shown above, decreases significantly with the charge density. Probably, the explosion emission velocity decreases as the pressure decreases, and metal-containing particles, therefore, are near each other for a longer time, colliding and joining each other at the same time. This hypothesis explains why the detonation of loose FeC_2O_4/PETN charge produces larger (on average) iron-containing particles than those produced by pressed charges

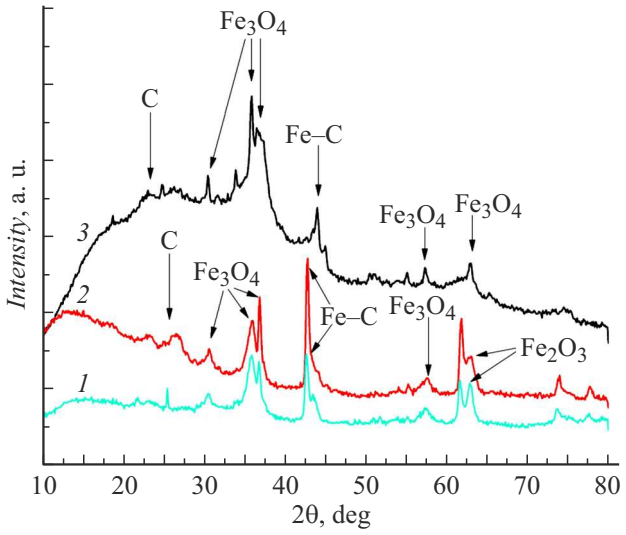

Figure 3. Diffraction patterns of detonation products: *1* — pressed 6% FeC_2O_4/PETN charge; *2* — pressed 3% FeC_2O_4/PETN charge; *3* — loose 3% FeC_2O_4/PETN charge.

with the same composition. At the same time, the absence of precursor concentration influence when the concentration changes by a factor of two in the pressed samples indicates that the material decomposition products of Fe(II) oxalate granules or their small agglomerates initially separated in space do not interact with each other during formation of nanoparticles. Therefore, the nanoparticle formation process presumably occurs during the detonation synthesis only on the scale of individual Fe(II) oxalate granules or their small agglomerates.

2.2. X-ray diffraction analysis of iron-containing explosion products

Diffraction patterns were made using the ARL X'TRA instrument with monochromatized CuK_α-radiation ($\lambda = 1.5418$ Å). Phases were identified by positions of diffraction peaks using the ICSD powder database.

Figure 3 shows diffraction patterns of condensed detonation products of FeC_2O_4/PETN charges. The diffraction patterns have maxima at $2\theta = 30.1$, 35.5, 37.1, 57.1 and 62.7° corresponding to reflexes $hkl = 220$, 311, 222, 511 and 440 of the Fe_3O_4 magnetite phase (PDF №19-629), and an intense maximum at $2\theta = 42.5°$ corresponding to reflex $hkl = 101$ in the iron carbide phase — carbon solid solution in iron with composition close to $Fe_{1.88}C_{0.12}$ (PDF №44-1293). Angular position of reflex (101) of iron carbide varies a little between samples (in the range from 42.5 to 45°), which is indicative of a small difference in carbon content in the sample carbide phase.

Diffraction peak splitting observed for the detonation products of pressed 3% FeC_2O_4/PETN and 6% FeC_2O_4/PETN charges in the far angle range ($2\theta = 60-65°$) and the change of peak intensity ratio at 35° indicate the presence of the γ-Fe_2O_3 maghemite phase (PDF №39-1346) in these samples that is represented by the diffraction peaks $hkl = 113$ and 044. An intense wide peak at $2\theta = 23-27°$ on the diffraction pattern of the detonation product of the loose 3% FeC_2O_4/PETN charge is assigned to graphite-like structure carbon. Intensity of this peak on the detonation product diffraction pattern of the pressed charge with the same composition is much lower. There is almost no such reflex on the diffraction pattern of a sample obtained from detonation of the pressed 3% FeC_2O_4/PETN charge. This suggests that the explosion of a PETN-based loose charge produces a much larger amount of crystalline carbon than the explosion of similar pressed charges. Content of amorphous carbon in the samples isn't detected by XPA and wasn't evaluated.

Mean sizes of the coherent scattering region (CSR) for each iron-containing particle phase in the detonation products of FeC_2O_4/PETN charges calculated using the Scherrer equation with accuracy of about 5–10 nm are listed in Table 4.

Thus, the detonation products of all FeC_2O_4/PETN charges contain,besides the detonation carbon, metallic iron particles, in which a small amount (~ 6 at.%) of carbon is dissolved, and Fe_3O_4 particles. The pressed charge detonation products also contain the γ-Fe_2O_3 maghemite particles. Contrast spots of the microphotographs of the FeC_2O_4/PETN detonation products are the images of the Fe–C, Fe_3O_4 and γ-Fe_2O_3 particles on the surfaces of which there are crystalline carbon layers with different thickness.

(II,III) Fe_3O_4 might have been caused (together with metallic iron) by disproportionation of iron oxide, primary decomposition product of FeC_2O_4,

$$4FeO \rightarrow Fe_3O_4 + Fe$$

and/or by its oxidation by oxygen contained in the system. Furthermore, some amount of the Fe_3O_4 crystallites might have occurred among the solid detonation products resulting from the shockwave damage of the explosion chamber walls. Fe(II) oxide may be a product of the later reduction of Fe_3O_4.

2.3. X-ray diffraction analysis of copper-containing explosion products

Figure 4 shows diffraction patterns for explosion products with copper-containing nanoparticles that are of quite complex type for analysis. Dashed lines in different colors show the expected phases. A black line and designation Cu-ox at $2\theta = 23.2$ and 30.3 show the diffraction maxima corresponding to $hkl = 110$ and 411 of Cu(II) oxalate with the general formula $CuC_2O_4 \cdot 0.5H_2O$ (PDF №48-1054), a red line at $2\theta = 25.1$, 31.7 and 35.7° shows the peaks $hkl = 111$, 021 and 113 of azurite with designation Cu-az and general formula $Cu_3(CO_3)_2(OH)_2$ (PDF №11-682), a cyan line at $2\theta = 26.5$ and 43.8° refers to the 3*R* graphite structure that is represented by peaks $hkl = 211$

Table 4. CSR sizes for various iron-containing phases in the detonation products of FeC_2O_4/PETN charges

Sample	3 wt.% FeC_2O_4/PETN (pressed)	6 wt.% FeC_2O_4/PETN (pressed)	3 wt.% FeC_2O_4/PETN (loose)
Fe−C CSR sizes, nm	22	18	20
Fe_3O_4 CSR sizes, nm	24	22	22
Fe_2O_3 CSR sizes, nm	7	11	–

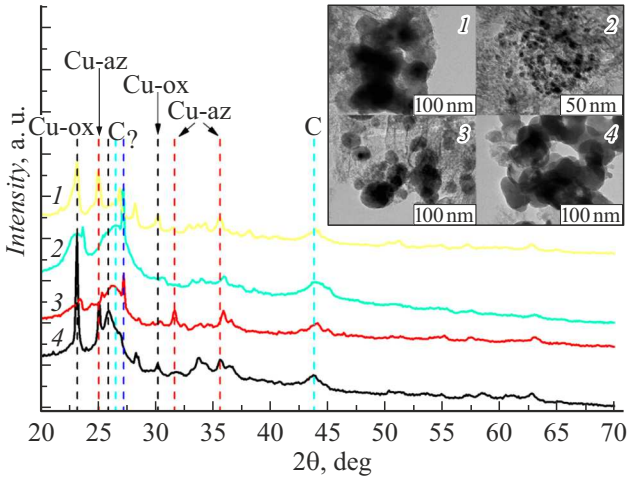

Figure 4. Diffraction patterns of the detonation products of: *1* — CuC_2O_4/hexogen charge; *2* — $Cu(CH_3COO)_2$/hexogen charge; *3* — $Cu(CH_3COO)_2$/PETN charge; *4* — CuC_2O_4/PETN charge.

and 100, respectively (PDF №26-1079). Moreover, the diffraction patterns show undesignated reflexes, in particular, an intense reflex at 27.25° (shown by a blue line) and other less intense reflexes. Phase composition for the obtained samples may be, if necessary, determined more accurately during future studies.

Mean CSR sizes for each copper-containing particle phase in the detonation products of Cu(II) oxalate/acetate and hexogen/PETN charges calculated using the Scherrer equation with accuracy of about 5−10 nm are listed in Table 5.

Diffraction patterns made for the CuC_2O_4/PETN and CuC_2O_4/hexogen samples show sharp high peaks corresponding to Cu-ox at 23°, 26° and 30° suggesting that the oxalates were not fully decomposed. However, for a hexogen-based sample, broadening of the major Cu-ox, peak base is observed which may suggest that both coarse and relatively fine Cu(II) oxalate particles are present. For the $Cu(CH_3COO)_2$/PETN and $Cu(CH_3COO)_2$/hexogen samples, the diffraction patterns also have wide Cu-ox peaks which may be indicative of a possible synthesis of fine oxalate nanoparticles within∼ 5−15 nm, and this peak is much more intense for the hexogen-based sample. Thus, the hexogen-based charge detonation products contain a much larger amount of nanodispersion Cu(II) oxalate, including the $Cu(CH_3COO)_2$/hexogen charge that didn't contain the oxalate initially.

The diffraction patterns made for the CuC_2O_4/PETN and CuC_2O_4/hexogen samples have peaks at 25°, 31° and 35° that correspond to the Cu-az phase or azurite phase. There are no major peaks of this phase on the diffraction patterns of the $Cu(CH_3COO)_2$/PETN and $Cu(CH_3COO)_2$/hexogen samples, consequently, azurite isn't formed during the detonation of copper acetate ES. However, some minor peaks occur, for example, for the $Cu(CH_3COO)_2$/hexogen sample at 31° that may result from overlapping of small peaks from various impurities or other phases. According to the XPA data, unlike the iron-containing samples, there are no metallic and metal-containing phases that are the thermal decomposition products, and Cu(II) oxalate and Cu(II) acetate. However, the Cu-az phase observed on the diffraction patterns of some samples shall be also decomposed in heating to form CuO. Notwithstanding that copper and copper oxide nanoparticles were not synthesized in this experiment series, the findings are of certain interest for defining the chemical reaction mechanism involving copper-containing compounds in explosion conditions.

Figure 4 also shows microphotographs of preserved explosion products of loose charges with copper-containing samples. As for samples with iron-containing precursors, detonation carbon constitutes a small fraction of condensed product.

The preserved explosion products of all copper-containing charges contain irregular particles and their aggregates with sizes from ones to 500 nm. Copper-containing precursors were presumably not fully decomposed during detonation and also formed more complex substances during reaction due to which copper-containing particles have their irregular shape. Therefore, the TEM data cannot be used to plot histograms by sizes as in the copper-containing particle case.

Also for the CuC_2O_4/PETN sample explosion products, structural analysis was carried out using the small-angle X-ray scattering technique. It has shown that explosion products consisted mainly copper-containing particles with complex morphology which can be seen on the microphotographs with copper. Clear difference with the small-angle X-ray scattering results is observed for iron-containing explosion products.

Table 5. CSR sizes for various copper-containing phases in the detonation products of PETN/hexogen and Cu(II) oxalate/acetate charges

Sample	CuC_2O_4/PETN	CuC_2O_4/hexogen	$Cu(CH_3COO)_2$/PETN	$Cu(CH_3COO)_2$/hexogen
Cu-ox CSR sizes, nm	41	25	15	5
Cu-az CSR sizes, nm	31	25	–	–

3. Main findings and conclusions

Decomposition of the $(10-20\,\mu m)$ FeC_2O_4 granules in the PETN explosion conditions produced ball-shaped nanoparticles of metallic iron (carbon-doped) and various iron oxides. Content of FeC_2O_4 in the pressed charges almost doesn't affect the kind of nanoparticle size distribution. The obtained data suggests that formation of iron-containing nanoparticles takes place within each individual precursor granule, i.e. the nanoparticle synthesis process during detonation occurs on a scale in the order of tens of micrometers due to high emission velocity and temperature reduction of explosion products. When the charge density decreases, the mean size and general view of particle size distribution vary significantly.

In PETN or hexogen explosion conditions, Cu(II) acetate was decomposed completely and Cu(II) oxalate was decomposed only partially. An unexpected result was that the decomposition products didn't contain metallic copper and CuO that are formed during the $Cu(CH_3COO)_2$ and CuC_2O_4 thermolysis.

Acknowledgments

The authors are grateful to N.Khrebtova and E.Klimiva, the students of the Specialized Educational and Research Center of Novosibirsk State University for the synthesis of fine crystalline $CuC_2O_4 \cdot 0.5H_2O$.

Conflict of interest

The authors declare that they have no conflict of interest.

References

[1] B.P. Tolochko, A.P. Tchernyshev, K.A. Ten, E.R. Pruuel, I.L. Zhogin, P.I. Zubkov, N.Z. Lyakhov, L.A. Lukyanchikov, M.A. Sheromov. Fizika metallov i metallovedenie (in Russian) **105**, 2 (145) (2008) (in Russian).

[2] V.V. Osipov, V.V. Platonov, V.V. Lisenkov, K.I. Demidova, S.V. Zayats, M.P. Zykova. ZhTF, **93** (10), 1481 (2023) (in Russian). DOI: 10.61011/JTF.2023.10.56287.124-23

[3] G.Partizan, B.Z. Mansurov, B.S. Medyanova, A.B. Koshanova, B.A. Aliev. ZhTF, **86** (11), 86 (2016) (in Russian). DOI: 10.21883/jtf.2016.11.43819.1763

[4] A.I. Sidorov, U.V. Yurina, O.A. Podsvirov. ZhTF **89** (7), 1079 (2019) (in Russian). DOI: 10.21883/JTF.2019.07.47803.2-19

[5] A.I. Ancharov, B.B. Bokhonov, P.I. Zubkov, P.I. Ivanov, A.M. Kartashov, N.Z. Lyakhov, L.A. Lukyanchikov, L.A. Merzhievsky, V.G. Svikh, K.A. Ten, V.M. Titov, B.P. Tolochko, M.R. Sharafutdinov, M.A. Sheromov. XVIII *Mezhdunarodnaya konferentsiya. Vozdeistvie intensivnykh potokov energii na veshchestvo.* Sb. dokl. Fizika ekstremal'nykh sostoyaniy veshchestva (2003), s. 97–98 (in Russian).

[6] A.O. Kashkarov, E.R. Pruuel, K.A. Ten, E.Yu. Gerasimov, S.I. Kremenko, I.A. Rubtsov, G.R. Dashapilov, P.A. Pyrjaev, B.L. Moroz. J. Phys.: Conf. Ser., **1147**, 012037 (2019).

[7] L.A. Lukyanchikpv, L.A. Merzhievsky, O.V. Evdokov, P.I. Zubkov, N.Z. Lyakhov, E.R. Pruuel, K.A. Ten, B.P. Tolochko, M.R. Sharafutdinov.*Ultradispersnye poroshki, nanostruktury, materialy: poluchenie. Svoistva primenenie.* IV Staverovskie chteniya. Tr.Vserossiiskoy nauchno-tekhnicheskoy konf., Krasnoyarsk. 2006, s. 74 (in Russian).

[8] Yi Lu, Zhenping Zhu, Zhenyu Liu. Carbon, **43** (2), 2005.

[9] H. Yan, T. Zhao, X. Li. Combust Explos Shock Waves, **51**, 495 (2005). DOI: 10.1134/S0010508215040152

[10] Ning Luo, Xiaojie Li, Yuling Sun, Xiaohong Wang. J. Alloys Compounds, **505** (1), 352 (2010). DOI: 10.1016/j.jallcom.2010.05.181

[11] A.V. Tchurikov, I.A. Leenson. Elektrokhim. energetika, **11**, 14 (2012) (in Russian).

[12] D.A. Pivovarov, Yu.Yu. Golubchikova, A.P. Ilyin. Izvestiya Tomskogo politekh. un-ta, **321** (3), 11 (2012) (in Russian)

[13] Zh. Lin, D. Han, Sh. Li. J. Thermal Analysis Calorimetry, **107**, 471 (2012).

[14] S.B. Sibocoza, M.J. Moloto, F. Mtunzi, N. Moloto. Asian J. Chem., **34**, 239 (2022).

[15] A.O. Kashkarov, E.R. Pruuel, K.A. Ten, E.Yu. Gerasimov, S.I. Kremenko, I.A. Rubtsov, G.R. Dashapilov, P.A. Pyrjaev, B.L. Moroz. J. Phys.: Conf. Series, **1147** (1), 012037 (2019). DOI: 10.1088/1742-6596/1147/1/012037

[16] A.P. Ershov, A.L. Kupershtokh. Fizika goreniya i vzryva, **3**, 118 (1986) (in Russian)

[17] L.A. Feigin, D.I. Svergun, G.W. Taylor. *Structure Analysis by Small-Angle X-Ray and Neutron Scattering* (Plenum Press, NY., 1987), 335 p.

[18] *Vychislenie parametrov detonatsii Tchepmena–Zhuge energeticheskikh materialov* Electronic source. Available at: https://ancient.hydro.nsc.ru/chem/gase_deton_ ref.php

Translated by E.Ilinskaya